# Pickup Ions beyond the Heliopause

V. Roytershteyn 1, N. V. Pogorelov 2,3, and J. Heerikhuisen 2,3, Space Science Institute, Boulder, CO 80301, USA; vroytershteyn spacescience.org

Department of Space Science, The University of Alabama in Huntsville, Huntsville, AL 35805, USA

Center for Space Plasma and Aeronomic Research, The University of Alabama in Huntsville, Huntsville, AL 35805, USA

Received 2018 October 11; revised 2019 June 14; accepted 2019 June 17; published 2019 August 13

#### **Abstract**

Fluxes of energetic neutral atoms (ENAs) with energies greater than 1 KeV measured by the *Interstellar Boundary Explorer* (*IBEX*) are predominantly created by charge exchange of interstellar neutral atoms with hot, nonthermal (pickup) ions. Since the properties of pickup ions (PUIs) depend on the place of their birth, they bear an imprint of the interaction between the solar wind (SW) and the local interstellar medium (LISM). Of special importance is a narrow "ribbon" of an enhanced ENA flux discovered by *IBEX*. While the origin of this ribbon is still under debate, various models attribute it to charge exchange between the LISM neutral atoms and PUIs just beyond the heliopause. In this work, we investigate the stability of PUI distributions inferred from global modeling of neutral atoms in the heliosphere using fully kinetic particle-in-cell modeling. The initial distribution consists of PUIs created from high-speed, low-temperature neutral atoms born in the supersonic SW ahead of the heliospheric termination shock (TS) and PUIs created from low-speed, high-temperature H atoms born between the TS and the heliopause. The simulations indicate that such distributions are unstable against quasi-parallel modes with fast growth timescales (of the order of one hour or less). The development of these instabilities may strongly modify the initial PUI distribution, leading, for example, to formation of a plateau in the direction parallel to the local magnetic field. These modes, however, saturate at relatively small amplitudes and do not lead to complete isotropization of the distribution on the timescales considered.

Key words: ISM: kinematics and dynamics - magnetic fields - solar wind - Sun: heliosphere

#### 1. Introduction

The problem of the solar wind (SW) interaction with the local interstellar medium (LISM) is one of the fundamental problems in heliophysics, which is made current by in situ measurements provided by Voyager 1 (V 1) and Voyager 2 (V 2) spacecraft. A variety of physical processes accompany this interaction. From the MHD perspective, when the SW collides with the LISM, a tangential discontinuity (the heliopause, HP) is formed. The HP separates the heliosphere from the LISM. The heliospheric magnetic field and the interstellar magnetic field (ISMF) are both parallel to the HP surface. The SW flow is decelerated to subfast magnetosonic velocities through the heliospheric termination shock (TS). The velocity magnitude and direction, as well as the ion temperature, in the unperturbed LISM are determined from the neutral He observations in the inner heliosphere by Ulysses (Witte 2004) and Interstellar Boundary Explorer (IBEX; Bzowski et al. 2015; McComas et al. 2015):  $V_{\infty}=26.4$ km s<sup>-1</sup> and  $T_{\infty} = 8000$  K. The pristine LISM plasma consists mostly of H atoms and protons, the densities of which are not directly measured. Similarly, no direct measurements of the ISMF vector,  $\mathbf{B}_{\infty}$ , exist in the unperturbed LISM. These quantities can be derived from numerical simulations that fit different observational data sets (see, e.g., Heerikhuisen & Pogorelov 2011; Heerikhuisen et al. 2014; Zirnstein et al. 2016). V 1 penetrated into the LISM in 2012 July and now is measuring the ISMF modified by the presence of the HP (Burlaga et al. 2013; Burlaga & Ness 2016) and plasma wave frequency, which is directly related to density (Gurnett et al. 2015). Thus, the magnetic field strength and direction, as well as plasma density near the HP are the measured quantities that can be reproduced by numerical simulations (Pogorelov et al. 2017a, 2017b).

Resonant charge exchange between interstellar neutrals and SW ions is an efficient kinetic process (the mean free path ranges from tens to hundreds of astronomical units) that creates secondary neutral atoms and nonthermal pickup ions (PUIs). The properties of newly created particles depend on the SW-LISM interaction region where a charge exchange occurs. For example, charge exchange in the supersonic SW inside the TS produces secondary H atoms that propagate outwards with the SW velocity, creating the so-called neutral SW. Secondary neutral atoms born in the inner heliosheath have lower bulk velocity, but much higher effective temperature. On the other hand, an ion created by charge exchange in the supersonic SW initially moves with the local ISM velocity. The SW motional electric field acts on this ion until its gyro-center velocity coincides with the ambient SW plasma velocity, creating a nonthermal PUI (Parker 1963: Vasvliunas & Siscoe 1976). In fact, no thermal equilibrium is reached as these PUIs convect with the SW.

PUIs are also produced in the LISM, when the pristine interstellar neutral atoms exchange charge with the ISM ions decelerated ahead of HP. These PUIs should then decelerate similarly to the parent ions and therefore play an important role in making the heliosphere less responsive to the asymmetrizing ISMF effect. In particular, the ISMF with strength of about 3  $\mu$ G would rotate the heliosphere dramatically (Pogorelov et al. 2007). This rotation is mitigated partially by the ram pressure of the decelerated PUIs for an obvious reason: there is more charge exchange in the area where the density of primary LISM ions is greater. For this reason, the ion density further increases, transferring more kinetic energy into thermal pressure (e.g., Pogorelov et al. 2011).

In this work, we are interested in energetic neutral atoms (ENAs), the flux of which is measured by the *IBEX* (e.g.,

McComas et al. 2017). The IBEX mission (McComas et al. 2009a) is the first space mission dedicated solely to the investigation of the SW-LISM interaction. IBEX performs fullsky observation of ENAs with two cameras with the combined energy range of 10 eV-6 keV. The lower energy corresponds to proton velocities of about  $44 \,\mathrm{km \, s^{-1}}$ . This means that pristine LISM neutral H atoms cannot be seen by IBEX unless it moves in the direction opposite to the LISM (Heerikhuisen & Pogorelov 2011). The highest energy corresponds to velocities of about 1000 km s<sup>-1</sup>. Bulk velocities of this magnitude are not observed during SW-LISM interaction, except perhaps in coronal mass ejections. However, thermal velocities of this order are possible beyond the TS. An interesting feature discovered by IBEX is the narrow region of enhanced ENA flux, which is now referred to as the IBEX ribbon. Before any explanation of this phenomenon was proposed, it was noticed that the directions toward the ribbon correlated with the line-ofsight directions perpendicular to the ISMF lines draping around the HP in the simulation of Pogorelov et al. (2009). One of the possible explanations of the ribbon flux was mentioned by McComas et al. (2009b) and Schwadron et al. (2009), and described in more detail by Heerikhuisen et al. (2010). It is based on the assumption that PUIs born in the LISM region in front of the HP due to charge exchange of the neutral SW H atoms with interstellar ions, if injected with a pitch angle close to 90° to the draped ISMF direction, preserve their anisotropy long enough to produce ENAs propagating toward IBEX in the plane perpendicular to B. This scenario is supported by numerical simulations, when anisotropy is assumed. We also note that the relative brightness of the ribbon is highest at energy ~1.1 keV, which corresponds to the speed of slow SW of roughly  $460 \,\mathrm{km \, s^{-1}}$ .

In this paper, we test the crucial assumption of this *IBEX* ribbon scenario, namely that the anisotropy of a realistic PUI distribution can be preserved long enough to experience another charge exchange. We use fully kinetic particle-in-cell (PIC) simulations to investigate the time evolution of the PUI distribution function in the outer heliosheath (outer) just outside of the HP. The initial distribution function is derived from the neutral H simulations performed by Heerikhuisen et al. (2016) and takes into account PUIs of the neutral SW and IHS.

#### 2. PUIs in the Outer Heliosphere

The ribbon mechanism developed by Heerikhuisen et al. (2010) requires that the PUI distribution function in the OHS preserves a certain degree of anisotropy for a sufficiently long time for a subsequent charge exchange to occur ( $\sim$ 2 yr for 1.1 keV H ions). This is not quite obvious because ring-beam distributions, typical for ions externally inserted into a background plasma, tend to scatter onto a shell distribution (Williams & Zank 1994).

Heerikhuisen et al. (2010) assumes that the ring-beam distribution is scattered onto a partial shell distribution depending on the injected pitch angle. In contrast, Chalov et al. (2010) neglects scattering, but appeals to magnetic mirroring effects that ensure spatial localization of injected PUIs. Mirroring also plays an essential role in the model of Giacalone & Jokipii (2015), who proposed a mechanism for producing ribbon-like enhancement of ENA flux that depends on PUI trapping in pre-existing turbulence. Schwadron & McComas (2013) proposed that the ribbon could be produced by

enhanced scattering and the resulting spatial retention of PUIs by locally generated waves. The stability of PUI distributions and the properties of self-generated fluctuations thus play an important role in many of the theories on the origin of the ribbon.

The question of stability of ring-like PUI distributions has been investigated by many authors over several decades. An informative summary of the earlier investigations, which primarily focused on cometary environments, could be found in Gary & Madland (1988). In particular, Gary & Madland (1988) demonstrated that the character of the dominant instability associated with ring-like PUI distributions changes as a function of PUI injection angle. Furthermore, they identified the finite temperature of the PUI ring as an important parameter that controls the nature of the most unstable mode at angles close to 90° (injection perpendicular to the local magnetic field). The discovery of the IBEX ribbon reinvigorated interest in the topic. Florinski et al. (2010) considered several model PUI distributions with parameters representative of the outer heliosphere, including  $\delta$ -function, partial shell, and distribution with a thermal spread in the direction perpendicular to the local magnetic field. By using linear theory and 1D hybrid simulations, Florinski et al. (2010) concluded that such PUI distributions tend to be unstable and will be scattered onto a thin shell on timescales of the order of a few days. Similar conclusions were reached by Liu et al. (2012), who considered gradual injection of a  $\delta$ -function distributed PUIs into 1D hybrid simulations. In contrast, Summerlin et al. (2014) used linear theory to identify parallel (with respect to the local magnetic field) spread of PUI distributions as a strongly stabilizing factor and demonstrated that finite temperatures of the ring beam, corresponding to beam widths as little as 1°, are sufficient to suppress parallel instabilities. Florinski et al. (2016) performed a more comprehensive scan of parameters to discover that a second unstable region exists for perpendicular pickup at larger parallel spreads. Florinski et al. (2016) also considered a wider class of distributions, allowing in particular for an oblique pickup, which corresponds to a drift along the magnetic field. Such distribution were found to be strongly unstable in the direction of Voyager 1, corresponding to the pickup angle of 69°, with the predicted levels of self-generated fluctuations significantly exceeding observation reported by Burlaga et al. (2015). All of these results are in agreement with the earlier analysis of Gary & Madland (1988). Florinski et al. (2016) also emphasized the role of statistical noise in the PIC simulations, demonstrating that an extremely large number of particles (up to 10<sup>6</sup> per cell) is required to suppress spurious growth. Niemeic et al. (2016) considered more realistic distributions of PUI and used fully kinetic particle-in-cell simulations to investigate the role of electron dynamics, albeit in simulations with very large relative density of PUIs. The results mostly agreed with those reported in Florinski et al. (2016), while additional PUI distributions were found to increase isotropization rates. Recently, Min & Liu (2018) showed that oblique modes, such as mirror or ion Bernstein, can still be active in the stability gap identified by Summerlin et al. (2014) and Florinski et al. (2016), resulting in parallel heating of the PUI distribution that eventually pushes it out of the stability region and triggers the onset of Alfvén/ion cyclotron instability.

In contrast to the investigations summarized above, Gamayunov et al. (2010) and Gamayunov et al. (2017) solved gyro-averaged

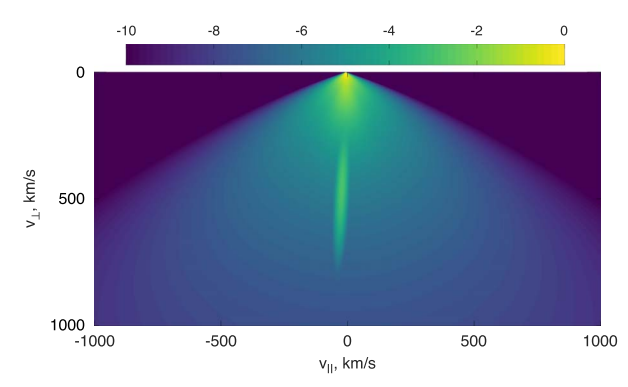


**Figure 1.** PUI distribution  $F = F_{\rm NSW} + F_{\rm IHSN,1} + F_{\rm IHSN,2}$  used in the present investigation. The color scale corresponds to the values of  $\log_{10} F/F_{\rm max}$ . In contrast to many previous investigations, we account for IHSN distributions with broad energy and pitch angle spread.

kinetic equations with a model pitch angle diffusion coefficient in the presence of both large-scale interstellar and self-generated turbulence with assumed properties. They concluded that the ribbon may still remain narrow because only a small part of the proton phase space distribution function can resonate with a locally generated ion cyclotron turbulence.

### 3. Model Description

#### 3.1. Simulation Methodology

Similarly to many previous investigations of the stability of PUI distributions, we focus on the initial development of PUI-driven instabilities during a relatively short interval of times and consider periodic domains in one and two spatial dimensions. Effects of wave propagation out of the interaction region, pre-existing turbulence of interstellar origin or driven by phenomena other than PUI, as well as effects associated with inhomogeneity in the background parameters (such as the direction and the magnitude of the magnetic field) are thus excluded from consideration.

The focus of the present investigation is two-fold. First, we are interested in the stability of the most realistic prediction to date for the distribution function of PUIs, which comes from a global modeling of neutral atom behavior in the heliosphere. The resulting distribution functions are considerably more complicated than simple ring-like distributions used in many of the previous studies. In particular, they are multicomponent, corresponding to PUIs of different origins. The second motivation is to investigate the role of short-wavelength oblique (with respect to the local magnetic field) kinetic instabilities in addition to comparatively well studied quasiparallel long-wavelength mode. Indeed, the PUI distributions predicted by global models (Heerikhuisen et al. 2016, see also Figure 1) contain populations with relatively small perpendicular velocities  $v_{\perp}$  that may be expected to excite shortwavelength turbulence, such as lower-hybrid oscillations (Mithaiwala et al. 2010), which can subsequently interact with populations with larger  $v_{\perp}$ . Furthermore, a recent investigation reported by Min & Liu (2018) found that even ring-like distributions with large-perpendicular velocity can be unstable to mirror and/or ion Bernstein modes that lead to significant modifications of the distribution.

In order to have a unified framework capable of describing all potential instabilities of interest, we utilize a fully kinetic

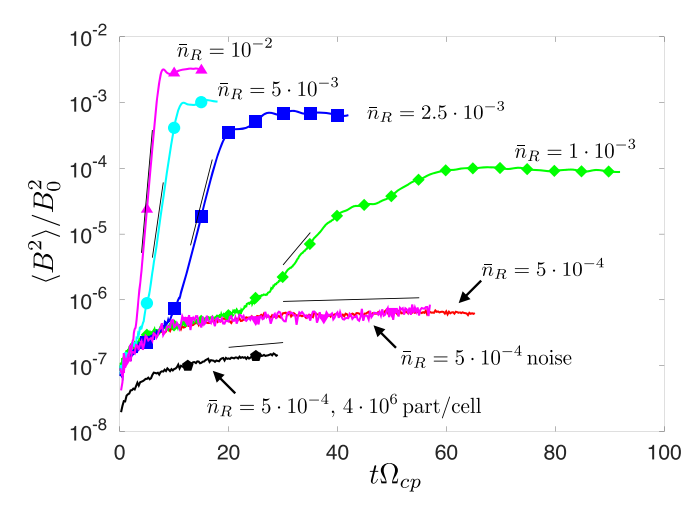


**Figure 2.** Evolution of an average energy power density in magnetic fluctuations for a case PUI distribution corresponding to a Gaussian ring. Results from 1D simulations with several values of the ring density are shown, as well as a control simulation with no instability. Straight lines indicate regions where curves are fitted to an exponential to compute linear growth rate (see Figure 3). Unless otherwise indicated, all of the simulations used 10<sup>6</sup> particles per cell.

Table 1
Parameters of PUI Distributions

Parameter	IHSN	NSW
$A (s^3 m^{-6})$	$9.71 \times 10^{-14}$	$3.19 \times 10^{-15}$
$B (s^3 m^{-6})$	$2.18 \times 10^{-12}$	
$V_{\parallel}  (\mathrm{km \ s}^{-1})$	-6.83	-22.1
$V_{\perp,1} \; ({\rm km \; s}^{-1})$	26.6	452
$V_{\perp,2} \; ({\rm km \; s^{-1}})$	1.19	•••
$\sigma_{a,1} \text{ (km s}^{-1}\text{)}$	26.1	54.3
$\sigma_{a,2} \text{ (km s}^{-1})$	0.99	•••
$\sigma_{b,1} \text{ (km s}^{-1})$	80.5	5.864
$\sigma_{b,2} \text{ (km s}^{-1})$	43.2	
$\theta$ (degrees)		2.84
$\kappa_1,  \kappa_2  (\mathrm{km  s}^{-1})$	3.5, 1.8	
$u_1, u_2 \text{ (km s}^{-1})$	100, 1.5	•••

formalism that describes both ion and electron species using the Vlasov equation. Such fully kinetic simulations were conducted using the general-purpose plasma simulation code VPIC (Bowers et al. 2008). The VPIC code solves relativistic Vlasov equations for both ions and electrons coupled to a full system of Maxwell's equations using an explicit PIC algorithm. While fully kinetic simulations in many ways represent a "first principle" approach to analysis of kinetic phenomena, the large separation of scales typical of most problems, including the OHS, necessitates a number of compromises. Specifically, explicit fully kinetic simulations must resolve spatial scales of the order of Debye length and temporal scales of the order of plasma frequency for numerical stability. In order to reduce simulation size and runtime to what is achievable on current computers, we use a frequently employed approximation where the mass ratio between protons and electrons is reduced from its physical value to  $m_p/m_e = 100$ . Another approximation is that the value of Alfvén speed is increased in relation to the speed of light to  $V_{\rm A}/c=1/60$ , compared to its actual value in the OHS  $V_{\rm A}/c\sim\times10^{-4}$  (see Section 3.2). Here

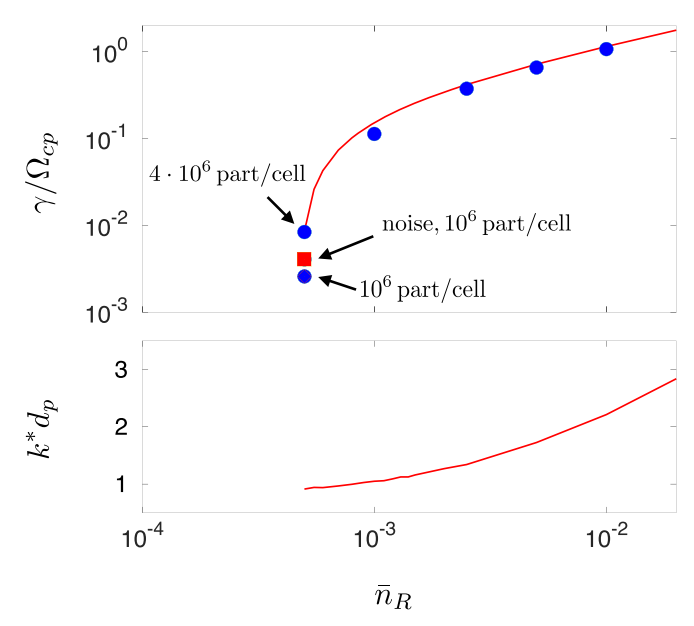


**Figure 3.** Top panel: the growth rate measured in the simulations of the Gaussian ring shown in Figure 2. Solid line shows the prediction of the linear theory obtained by a numerical solution of Equation (5). Bottom: the wavenumber  $k^*$  corresponding to the maximum growth rate from the linear theory.

 $V_{\rm A} = B_0 / \sqrt{4\pi n_b m_p}$ ,  $B_0$  is the uniform background magnetic field,  $n_b$  is the number density of the background plasma, and  $m_p$  is the proton mass. The distribution functions of PUI are rescaled such that characteristic values of PUI velocities normalized to Alfvén speed,  $v_{\parallel}/V_{\rm A}$  and  $v_{\perp}/V_{\rm A}$ , in the simulation are the same as the OHS values. Here  $\parallel$  and  $\perp$  refer to the direction of the local magnetic field. Since the values of  $\beta_s = 8\pi n_s T_s/B_0^2$  for background protons and electrons with temperatures  $T_s$  and density  $n_s$  are chosen to also correspond to their values in OHS, this implies that the ratio between characteristic velocities of PUI and the thermal speed of background protons in the simulation has the same value as the corresponding ratio in the OHS. We have conducted (necessarily limited) scaling studies, as well as linear analysis to verify that these approximations do not alter the physics of relevant instabilities.

A significant issue for particle simulations of PUI dynamics is the presence of statistical fluctuations (noise). The amplitude of such fluctuations is greatly exaggerated in the simulations relative to the real plasma due to a relatively small number of computational particles used to sample the phase space and due to the presence of computational grid. The numerical noise introduces enhanced numerical diffusion and other unwanted numerical effects. In order to suppress the noise to acceptable levels, we use an unconventionally large number of particles per cell in the simulations—up to  $4 \times 10^6$  for each species in 1D simulations and up to  $4 \times 10^4$  for each species in 2D simulations. We have also conducted a number of control simulations with the parameters corresponding to the cases of interest, but where the primary instabilities cannot develop since the most unstable wavenumbers are excluded by the choice of the simulation domain. Such simulations allow us to unequivocally assess the role of numerical effects. Finally, the majority of the simulations presented here were conducted for a range of PUI densities in order to obtain predictions for a wide range of parameters.

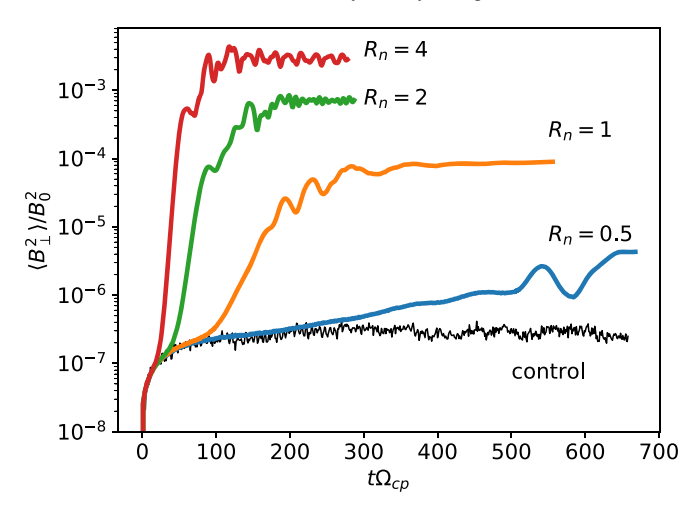


**Figure 4.** Evolution of average energy density in magnetic fluctuations for the PUI distributions given by Equations (1–3). Results from 1D simulations with several values of relative density enhancement factor  $R_n$  are shown, as well as a control simulation with no instability. The corresponding relative densities of PUIs are given in Table 2.

 Table 2

 Relative Densities of PUI Distributions Used in This Study

$\overline{R_n}$	$ar{n}_{ ext{NSW}}$	$ar{n}_{\mathrm{IHSN},1}$	$ar{n}_{\mathrm{IHSN},2}$
0.5	$1.8 \times 10^{-4}$	$4.3 \times 10^{-4}$	$5.0 \times 10^{-4}$
1	$3.6 \times 10^{-4}$	$8.6 \times 10^{-4}$	$1.0 \times 10^{-3}$
2	$7.3 \times 10^{-4}$	$1.7 \times 10^{-3}$	$2.0 \times 10^{-3}$
4	$1.5 \times 10^{-3}$	$3.4 \times 10^{-3}$	$4.0 \times 10^{-3}$

**Note.** The density of the background plasma is assumed to be  $n_p = 0.1$ .

## 3.2. Initial Conditions

The initial distributions of PUI correspond to those reported by Heerikhuisen et al. (2016), and are summarized here for completeness of the presentation. The PUI distribution consists of three components representing PUI that originated from neutral solar wind (NSW) or inner heliosheath neutrals (IHSN)

$$F_{\text{NSW}}(\nu_{\parallel}, \nu_{\perp}) = R_n A \exp \left[ -\left( \frac{\nu_{\perp} - V_{\perp, 1}}{2\sigma_{a, 1}} \cos \theta - \frac{\nu_{\parallel} - V_{\parallel}}{2\sigma_{a, 1}} \sin \theta \right)^2 - \left( \frac{\nu_{\perp} - V_{\perp, 1}}{2\sigma_{b, 1}} \sin \theta + \frac{\nu_{\parallel} - V_{\parallel}}{2\sigma_{b, 1}} \cos \theta \right)^2 \right]$$

$$(1)$$

$$F_{\text{IHSN},1} = R_n A \exp \left[ -\left( \frac{v_{\parallel} - V_{\parallel}}{\sigma_{a,1} v_{\perp} / u_1} \right)^2 \right]$$

$$\times \left[ 1 + \frac{1}{\kappa_1 - 3/2} \left( \frac{v_{\perp} - V_{\perp,1}}{\sigma_{b,1}} \right)^2 \right]^{-\kappa_1 - 1/2}$$

$$(2)$$

$$F_{\text{IHSN},2} = R_n B \exp \left[ -\left( \frac{v_{\parallel} - V_{\parallel}}{\sigma_{a,2} v_{\perp} / u_2} \right)^2 \right]$$

$$\times \left[ 1 + \frac{1}{\kappa_2 - 3/2} \left( \frac{v_{\perp} - V_{\perp,2}}{\sigma_{b,2}} \right)^2 \right]^{-\kappa_2 - 1/2} .$$

$$(3)$$

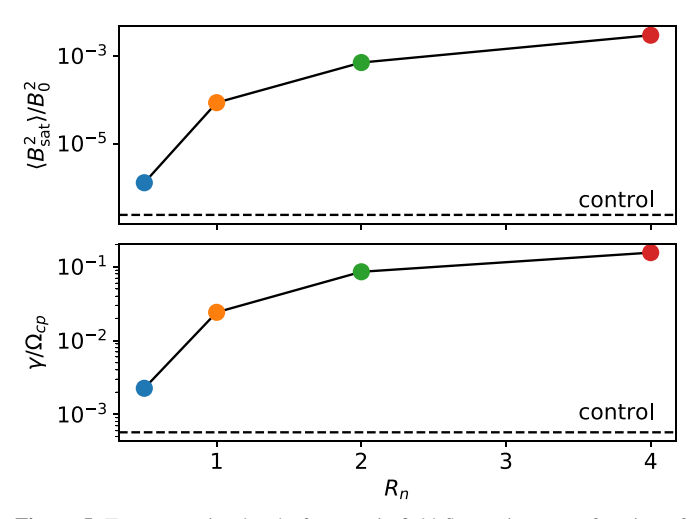


**Figure 5.** Top: saturation level of magnetic field fluctuations as a function of the density enhancement factor  $R_n$  for the simulations shown in Figure 4. Bottom: the growth rate measured in the simulations during the period of exponential growth.

The normalized parameters of the distributions are summarized in Table 1 and the distribution  $F = F_{\rm NSW} + F_{\rm IHSN,1} + F_{\rm IHSN,2}$  is illustrated in Figure 1. The IHS neutral atom distribution function is represented here as a sum of two functions, one for the low-energy core and another for the high-energy tail. The overall prefactor  $R_n$  is used to control relative density of PUIs in the simulations. We assume background plasma density  $n_p = 0.1~{\rm cm}^{-3}$ . The temperature and magnetic field of the background plasma enter only through plasma  $\beta$ . We consider  $B = 5 \times 10^{-6}~{\rm G}$  and  $T = 3.5 \times 10^4~{\rm K}$ , corresponding to  $\beta_e = \beta_p = \beta \approx 0.49$ . The plasma is assumed to be quasineutral, so that the electron density is equal to the total (background + PUI) proton density.

### 4. Results

#### 4.1. Stability of Model Ring-like Distributions

In order to both set the stage for the forthcoming discussion and to test the ability of the simulation approach to capture the essential physics of PUI evolution, we first examine a relatively well studied case. Specifically, we consider a single PUI distribution that is a Gaussian ring in the velocity space

$$F_R(\nu_{\parallel}, \nu_{\perp}) = A \exp \left[ -\frac{(\nu_{\perp} - V_0)^2 - \nu_{\parallel}^2}{\nu_R^2} \right].$$
 (4)

We consider the case previously examined by Summerlin et al. (2014), specifically a three-component plasma with the temperature of background populations  $T_e = T_p = 2 \times 10^4 K$ , background plasma density  $n_p = 0.1$  particles per cubic centimeter, the ring "temperature"  $T_r = m_p v_R^2/2 = 2000$  K, mean magnetic field  $B_0 = 2.5 \times 10^{-6}$  G, and characteristic velocity of the ring particles  $V_0 = 400$  km s<sup>-1</sup>  $\approx 23 V_A$ .

We conducted a series of simulations with varying PUI density  $n_{\text{PUI}} = \int d^3 v \, F_R(v)$ . All of the simulations utilize the scaling approach discussed in Section 3.1 and are conducted in one spatial dimension with the following numerical parameters: domain length  $L = 2\pi/k^*$ , where  $k^*$  is the wavenumber corresponding to the fastest growing mode (see below), spatial resolution  $\delta x$  corresponding approximately to 1 Debye length,

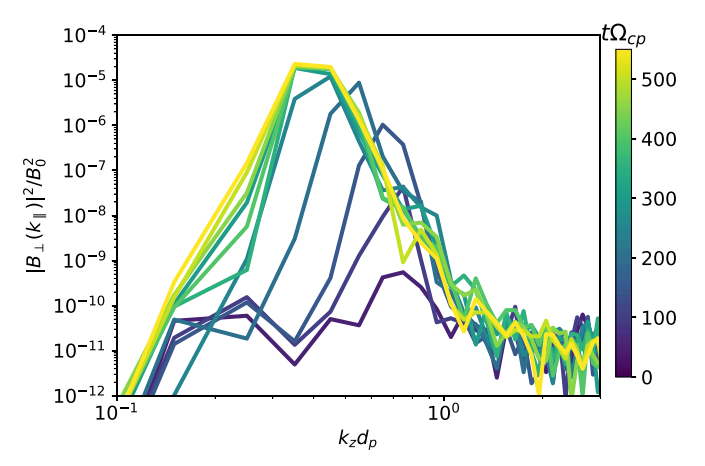


**Figure 6.** Time evolution of the k-spectrum of magnetic fluctuations in the 1D case with  $R_n = 1$ . Curves of different colors correspond to increasing times, as indicated by the color scale on the right.

and time step  $\delta t \approx \delta x/c$ . The number of particles per cell per species is  $10^6$  for all simulations, except for the case with the lowest (realistic) relative density of PUIs  $\bar{n}_R \equiv n_{\rm PUI}/n_p = 5 \times 10^{-4}$ , where simulations with both  $10^6$  and  $4 \times 10^6$  particles per cell per species were conducted.

Figure 2 shows the evolution in time of mean-squared amplitude of magnetic field perturbations  $\langle \delta B(t)^2 \rangle$  normalized to the value of background magnetic field  $B_0^2$ . Here  $\langle \dots \rangle$  refers to an average over the spatial domain. For each considered case, statistical fluctuations are established at early times, leading to a rapid increase in the level of fluctuations  $\langle \delta B^2 \rangle$  from nearly zero to its equilibrium value on timescales of a few inverse cyclotron frequencies. Eventually, the dominant instability grows out of the noise, leading to a period of exponential growth in  $\langle \delta B^2 \rangle$ , which is followed by saturation of the primary instability.

For parallel-propagating modes, the linear growth rate of the instabilities could be computed from an exact dispersion relation (Summerlin et al. 2014)

$$1 - \frac{k_{\parallel}^{2} c^{2}}{\omega^{2}} + \pi \sum_{s} \frac{\omega_{ps}^{2}}{\omega^{2}} \int \frac{v_{\perp}^{2} dv_{\perp} dv_{\parallel}}{\omega - k_{\parallel} v_{\parallel} \pm \Omega_{cs}}$$

$$\times \left[ (\omega - k_{\parallel} v_{\parallel}) \frac{\partial F}{\partial v_{\perp}} + k_{\parallel} v_{\perp} \frac{\partial F}{\partial v_{\parallel}} \right] = 0.$$
(5)

Here  $\Omega_{cs} = q_s B_0/(m_s c)$  is the cyclotron frequency of species s and  $\omega_{ps} = (4\pi n_s q_s^2/m_s)^{1/2}$  is their plasma frequency. Figure 3 demonstrates the growth rate measured during the period of exponential growth in the simulations (symbols) as well as a numerical solution of Equation (5) with the distribution function given by Equation (4) (solid curves). Overall, the simulations reproduce the expected growth rate very well, especially at higher values of the relative density. As the relative density of PUIs is reduced, the growth rate rapidly diminishes. At the lowest considered value  $\bar{n}_R = 5 \times 10^{-4}$ , the statistical noise in the simulation with 10<sup>6</sup> particles per cell strongly affects the results. However, simulations with  $4 \times 10^6$ particles per cell for each species accurately capture the growth rate. The wavenumber  $k^*$  corresponding to the maximum growth rate, as predicted by Equation (5), is shown in the bottom panel in Figure 3 as a function of the relative density  $\bar{n}_R$ .

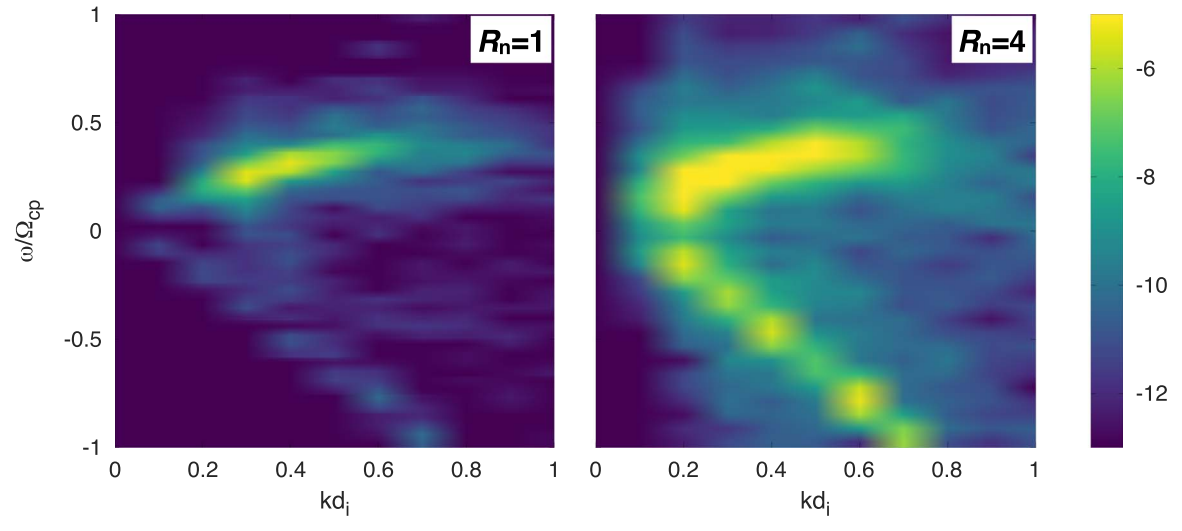


Figure 7. Wavenumber-frequency spectrum of magnetic field fluctuations in cases with  $R_n = 1$  (left) and  $R_n = 4$  (right). The color corresponds to  $\log_{10}|B_{\perp}(\omega, k_{\parallel})|^2/B_0^2$ .

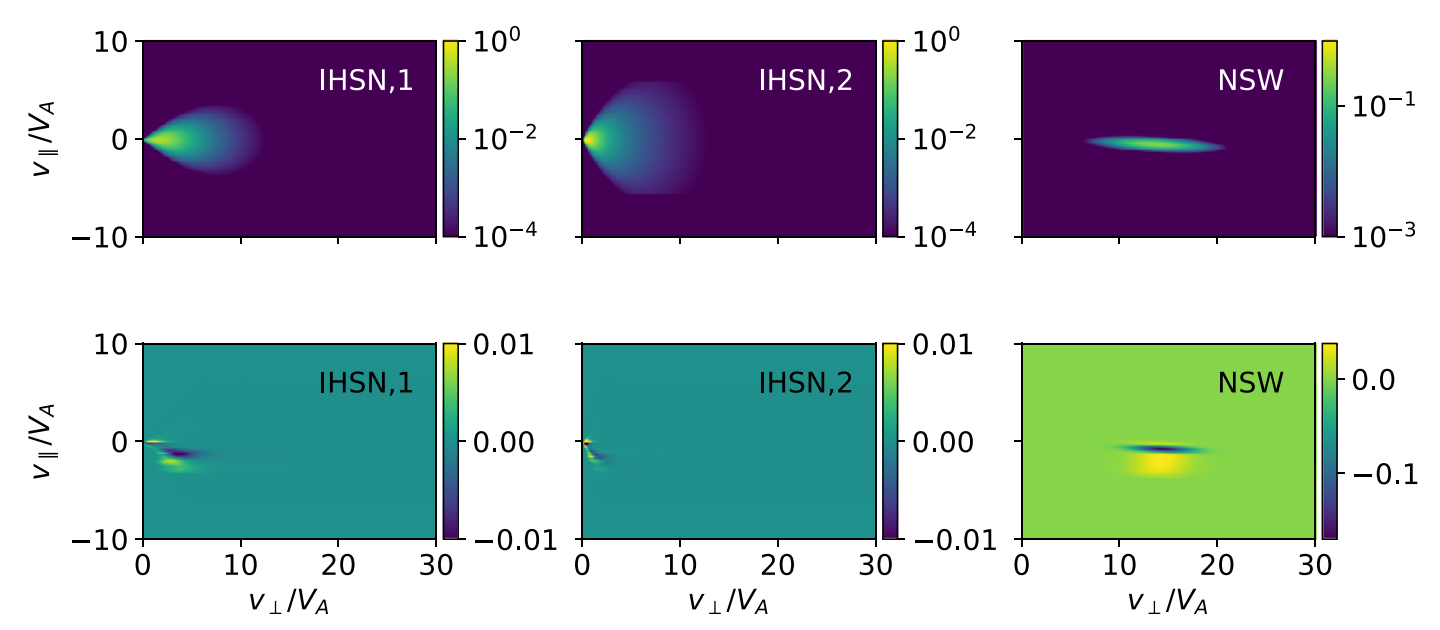


Figure 8. Top row: initial distribution function  $F(v_{\parallel}, v_{\perp})$  from the 1D simulation with  $R_n = 1$  for populations IHSN<sub>1</sub>, IHSN<sub>2</sub>, and NSW; bottom row: change in the distribution functions  $F(v_{\parallel}, v_{\perp}, t) - F(v_{\parallel}, v_{\perp}, 0)$  for the three populations at  $t\Omega_{cp} \approx 550$ .

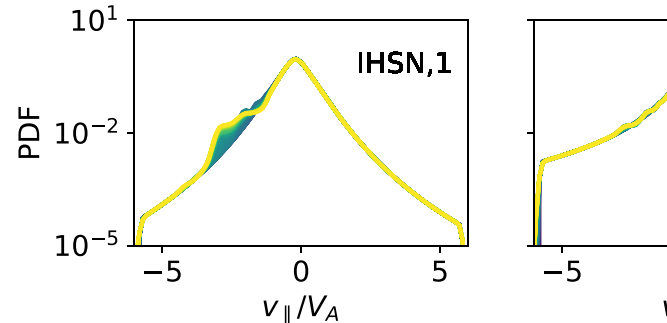
The spectrum of instabilities tends to shift toward longer wavelength with decreasing  $\bar{n}_r$ .

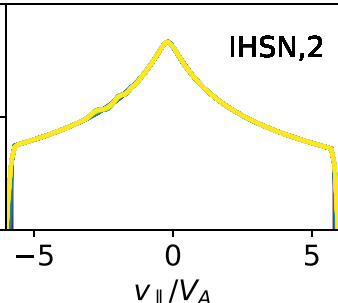
Overall, the results of the analysis presented here demonstrate that the chosen scaling approach and the adopted numerical methods are capable of accurately describing the considered (stringent) test case with good accuracy. Having established the appropriateness of the simulation methodology, we now turn our attention to the main subject of the paper—stability of the PUI distributions inferred from a global model, as given by Equations (1)–(3).

# 4.2. Stability of Distributions Predicted by MS-FLUKSS Global Model: 1D Simulations

The primary PUI-driven instabilities are expected to be field-aligned. To study these instabilities, we have conducted a number of 1D simulations with varying PUI density in domain

of length  $L=20\pi d_p$  with spatial resolution of approximately one Debye length. Here  $d_p=c/\omega_p=cm_p^{1/2}/(4\pi n_p e^2)^{1/2}$  is the proton inertial length. Unless otherwise specified, the number of particles per cell is  $10^6$  for each species. The relative density of PUIs was varied in the range  $R_n=0.5$ –4, where  $R_n$  is the multiplier controlling PUI density in Equations (1)–(3). This corresponds to the relative density of the NSW component  $\bar{n}_{\rm NSW}\approx (1.8$ – $15)\times 10^{-4}$  (see Table 2). Figure 4 demonstrates growth of magnetic field fluctuations in time. The simulations with  $R_n=1$  and  $R_n=0.5$  show considerably slower growth of the fluctuations relative to the cases with  $R_n\gtrsim 2$ , which is consistent with the behavior of simple ring distributions discussed in Section 4.1. Also shown in Figure 4 is the behavior of fluctuation power in a control simulation with parameters corresponding to  $R_n=1$  case, but short spatial extend that excludes the range of the most unstable





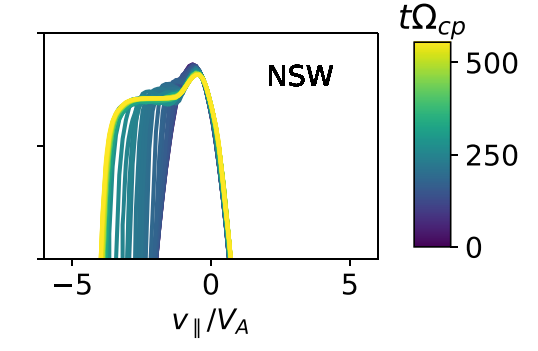
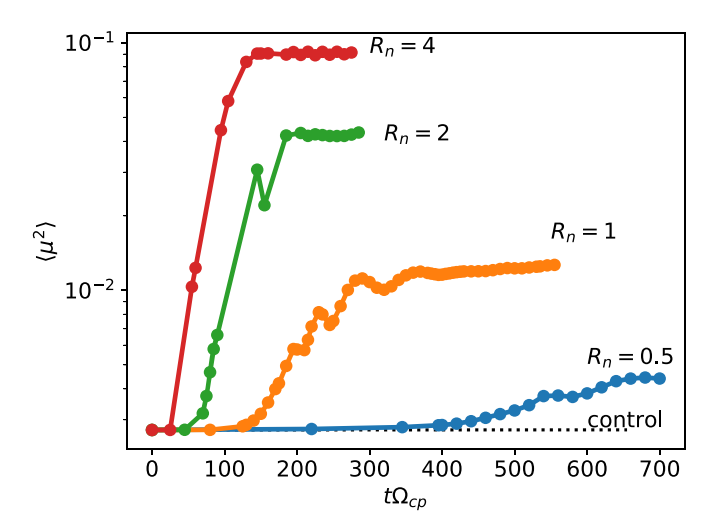


Figure 9. Time evolution of the reduced distribution function  $\bar{F}(v_{\parallel})$  for the three PUI populations in the 1D simulation with  $R_n = 1$ . Curves of different color correspond to increasing time.



**Figure 10.** Evolution of  $\langle \mu^2 \rangle = \langle \cos^2 \theta \rangle$  for the 1D simulations with  $R_n = (1 \dots 4)$ , as well as for the control simulation.

wavelengths. Such simulation allows us to assess the role of numerical effects, including that of the statistical noise. It is apparent that even the simulation with the lowest considered density  $R_n=0.5$  is well resolved in the sense that fluctuation amplitudes significantly exceed the background noise. The growth rate during the phase of exponential growth as well as an approximate saturation level of instabilities are summarized in Figure 5 as a function of the density enhancement factor  $R_n$ . The most important conclusion from this analysis is that the growth rate is large even for the lowest considered density. Indeed,  $\gamma/\Omega_{cp}\sim 2.4\times 10^{-2}$  for the  $R_n=1$  case, corresponding to approximately  $\gamma\sim 4.1~{\rm hr}^{-1}$  for the nominal conditions considered here. At the same time, the linear growth of the primary instability terminates at relatively low levels of the fluctuation magnetic field, with r.m.s. values of fluctuations  $\langle \delta B^2 \rangle^{1/2} \approx 9.2\times 10^{-3}B_0$ , corresponding to  $B_0\approx 4.6\times 10^{-8}$  G for the case  $R_n=1$ .

The frequency and wavenumber spectra of the instabilities are examined in more detail in Figures 6 and 7. The frequency spectra are computed by performing Fast Fourier Transforms of magnetic field components saved with temporal resolution of  $\delta T_d \approx 1/\Omega_{cp}$ , enabling computation of high-resolution k-spectra with maximum resolved temporal frequency of  $\omega_{\rm max} \approx \pi \Omega_{cp}$ . As is apparent from Figure 7, two separate, oppositely propagating modes with comparable wavenumbers

are present when the relative density of PUI is sufficiently high. One of the modes is on the magnetosonic/whistler branch and the other is of Alfvén ion cyclotron type (Gary & Madland 1988; Florinski et al. 2016). This mode is dominant in the  $R_n = 1$  case, while in the  $R_n = 4$  case, the amplitudes of the two modes are comparable. As the primary instability grows, a relatively steep spectrum of modes develops (see Figure 6).

The effects of the initial development of instabilities on distribution function of PUIs is examined in Figure 8, which shows the change in the distribution function relative to the initial distributions for the three PUI distributions in the  $R_n=1$  case. Both the resonance nature of the instability and its predominant effect, scattering of the NSW particles in  $v_{\parallel}$ , are apparent. At the end of the simulation, the NSW population is significantly distorted, as is well illustrated by Figure 9, which shows time evolution of reduced distributions. The most notable feature of these plots is the development of a characteristic plateau, which is most pronounced in the NSW distribution, but is present in IHSN distributions as well.

Ultimately, the quantity that is the most significant for the theories of the *IBEX* ribbon is the angular width of the PUI distribution. Figure 10 illustrates evolution of the mean-squared pitch angle  $\langle \mu^2 \rangle$ , where  $\mu = \cos \theta$  and  $\tan \theta = v_{\parallel}/v_{\perp}$ . The fluctuations lead to significant increase in  $\mu^2$  relative to the initial population on the timescales of the instability development. However, the NSW distribution remains well localized in pitch angle on the timescales considered. It is important to emphasize that the present investigation focuses only on the initial stages of development of the PUI-driven instabilities on timescales corresponding to several hours. During this time, primary instabilities grow rapidly and saturate. The pitch angle may in principle continue to (slowly) grow on a much longer timescale due to quasi-linear type diffusion in the wave field of the PUI-generated or externally injected turbulence.

# 4.3. Stability of Distributions Predicted By MS-FLUKSS Global Model: 2D Simulations

In order to investigate the possible development of oblique modes and their influence on PUI distributions, we have conducted a series of 2D simulations with parameters similar to those used in Section 4.2. Since using  $10^6$  particles per cell per species would make the computational cost of 2D simulations prohibitively large, we focus on the case with larger relative density,  $R_n \approx 1.6$  and larger  $\beta = 0.86$ . A large comparative study conducted in 1D indicated that the dynamics of the

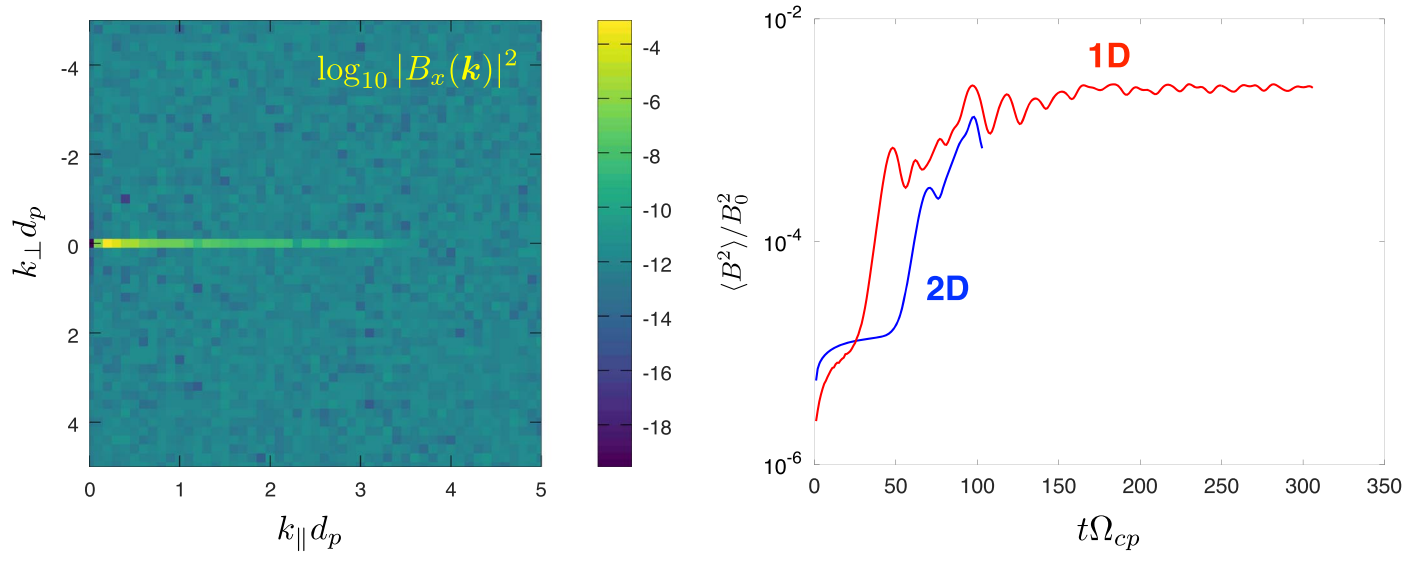
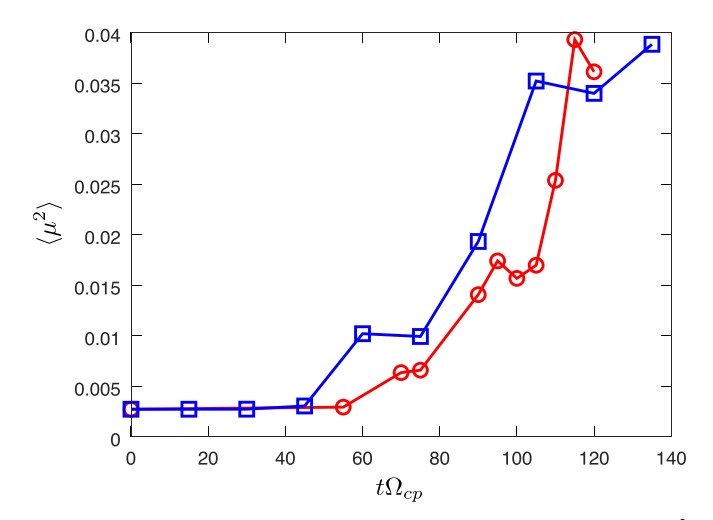


Figure 11. Summary of the results from 2D simulations. Left: spectrum of magnetic fluctuations  $|B_{\perp}(k_{\perp}, k_{\parallel})|^2$  in the simulation with  $R_n \approx 1.6$ ,  $\beta = 0.86$ . Right: dependence of the r.m.s. amplitude of fluctuations on time for 2D case and a corresponding 1D case.

system are qualitatively close to those in the simulations considered in the previous section. Furthermore, a convergence study has been performed in 1D confirming that simulations with  $4 \times 10^4$  particles per cell for each species adequately resolve mode growth and the evolution of the PUI distributions for this case. A corresponding 2D simulation has domain size  $L_v \times L_z = 10\pi d_p \times 20\pi d_p$ , 2048 × 4096 cells, 4 × 10<sup>4</sup> particles per cell per species, time step  $\delta t \ \omega_{pe} \approx 0.1$ , and other parameters similar to those reported for 1D simulations in Section 4.2. The most important result of the performed simulations is that no electromagnetic oblique modes of significant amplitude have been detected, at least in the range of wavenumbers resolved by the simulation domain (see Figure 11). The primary mode grows with a similar rate (albeit after some delay, which may be explained by a different spectrum of noise between 1D and 2D cases) and saturates at a similar amplitude compared to the corresponding 1D case. All other features of the evolution also appear similar between 2D and 1D cases. This is further demonstrated in Figure 12, which shows evolution of  $\mu^2$  for the NSW population and compares it against a similar 1D simulation. While very low-amplitude oblique electromagnetic modes and somewhat more pronounced high-frequency electrostatic fluctuations (corresponding to electron Bernstein and X modes) are present in the system, they do not appear to have a significant impact on the evolution of the PUI distribution or the growth of the primary modes.

### 5. Summary and Discussion

Current understanding of the *IBEX* ribbon, an enhancement of  $\sim$ 1 KeV ENA flux detected by *IBEX* spacecraft, is based on the assumption that PUIs born in the LISM region in front of the HP preserve their anisotropy on timescales of the order of two years, which is long enough to produce, by secondary charge exchange, ENAs propagating toward detection points. At the same time, highly non-Maxwellian distributions of PUIs are known to be unstable to a variety of plasma instabilities that tend to isotropize the distributions. In this paper, we used local high-resolution fully kinetic PIC simulations to investigate the



**Figure 12.** Comparison of the mean angular width of NSW populations  $\langle \mu^2 \rangle$  between a 2D simulation with  $R_n \approx 1.6$  and  $\beta = 0.86$  (red circles) and a 1D case with the same density, but  $10^6$  particles per cell (blue squares).

time evolution of the PUI distribution function under parameters corresponding to the outer heliosheath, a region just outside of the HP. In contrast to several previous investigations, we used as a starting point PUI distribution functions inferred from a global kinetic model of neutral H evolution presented by Heerikhuisen et al. (2016). Such distributions contain several distinct populations, differentiated by their origin in either NSW or inner heliosheath (IHSN).

The major conclusion of this work is that the distribution functions presented in Heerikhuisen et al. (2016) are unstable to quasi-parallel electromagnetic instabilities that grow on time-scales of an hour or less. The instabilities are driven primarily by the NSW population, but interact resonantly with the PUIs of all populations. The dominant effect of the instabilities is the formation of a plateau in the distribution function, rather than pitch angle scattering. The instabilities and the associated modifications of the PUI distributions saturate at amplitudes that depend on the relative density of the PUI distributions.

Crucially, in all of the simulations considered, the NSW PUI distributions preserved strong anisotropy on the considered timescales. Thus the results presented here are generally consistent with the assumptions made by Heerikhuisen et al. (2010), although they could not yet be considered a definitive proof, primarily due to the short timescales analyzed. In general, these results should further inform various hypotheses on the origin of the *IBEX* ribbon, since many of them invoke anisotropy of PUI distributions and/or interaction of the PUIs with self-generated waves.

The 2D simulations conducted for this study did not exhibit oblique electromagnetic instabilities with significant amplitudes. While electromagnetic oblique modes were detected, they had amplitudes near the noise level of the simulations and significantly less than the quasi-parallel modes. The simulations also revealed the existence of quasi-perpendicular electrostatic modes with frequencies exceeding electron cyclotron frequencies. These modes, however, do not appear to have any appreciable effect on the PUI distributions.

It should be emphasized that the presented investigation focused on initial, fast processes operating on time intervals much shorter than characteristic timescales of the charge exchange. On much longer timescales, even significantly weaker instabilities may have a significant effect. Furthermore, the PUIs can continue to interact with both the turbulence generated by the fast initial instabilities and that injected into the system by other processes (e.g., interstellar turbulence) over much longer timescales. Modeling of such interactions may require consideration of the global effects, including global propagation of both PUIs and the wave modes, as well as nonlinear interactions between the fluctuations.

This work was supported by NASA grants 80NSS C18K1649NS and NNX14AJ53G at Space Science Institute and 80NSSC18K1649NS, NNX14AJ53G, NNX14AF43G, NNX15A N72G, and NNX16AG83G at the University of Alabama, Huntsville. This work was also partially supported by the *IBEX* mission as a part of NASA's Explorer program. We acknowledge NSF PRAC awards ACI-1614664 and OAC-1811176, as well as related computer resources from the Blue Waters sustainedpetascale computing project, which is supported by the National Science Foundation (awards OCI-0725070 and ACI-1238993) and the state of Illinois. Furthermore, the work utilized computational resources provided by the NASA High-End Computing Program through the NASA Advanced Supercomputing Division at Ames Research Center and the allocation on Stampede provided by NSF through XSEDE project MCA07S033.

#### **ORCID iDs**

V. Roytershteyn https://orcid.org/0000-0003-1745-7587 N. V. Pogorelov https://orcid.org/0000-0002-6409-2392 J. Heerikhuisen https://orcid.org/0000-0001-7867-3633

#### References

```
Bowers, K. J., Albright, B. J., Yin, L., Bergen, B., & Kwan, T. J. T. 2008,
   PhPl, 15, 055703
Burlaga, L. F., Florinski, V., & Ness, N. F. 2015, ApJL, 804, L31
Burlaga, L. F., & Ness, N. F. 2016, ApJ, 829, 134
Burlaga, L. F., Ness, N. F., & Stone, E. C. 2013, Sci, 341, 147
Bzowski, M., Swaczyna, P., Kubiak, M. A., et al. 2015, ApJS, 220, 28
Chalov, S. V., Alexashov, D. B., McComas, D., et al. 2010, ApJL, 716, L99
Florinski, V., Heerikhuisen, J., Niemiec, J., & Ernst, A. 2016, ApJ, 826, 197
Florinski, V., Zank, G. P., Heerikhuisen, J., Hu, Q., & Khazanov, I. 2010, ApJ,
Gamayunov, K., Heerikhuisen, J., & Rassoul, H. 2017, ApJ, 845, 63
Gamayunov, K., Zhang, M., & Rassoul, H. 2010, ApJ, 725, 2251
Gary, S. P., & Madland, C. D. 1988, GeoRL, 93, 235
Giacalone, J., & Jokipii, J. R. 2015, ApJL, 812, L9
Gurnett, D. A., Kurth, W. S., Stone, E. C., et al. 2015, ApJ, 809, 121
Heerikhuisen, J., Gamayunov, K. V., Zirnstein, E. J., & Pogorelov, N. V. 2016,
    pJ, 831, 137
Heerikhuisen, J., & Pogorelov, N. V. 2011, ApJ, 738, 29
Heerikhuisen, J., Pogorelov, N. V., Zank, G. P., et al. 2010, ApJL, 708,
Heerikhuisen, J., Zirnstein, E. J., Funsten, H. O., Pogorelov, N. V., &
   Zank, G. P. 2014, ApJ, 784, 73
Liu, K., Möbius, E., Gary, S. P., & Winske, D. 2012, JGRA, 117, B09205
McComas, D. J., Allegrini, F., Bochsler, P., et al. 2009a, SSRv, 146, 11
McComas, D. J., Allegrini, F., Bochsler, P., et al. 2009b, Sci, 326, 959
McComas, D. J., Bzowski, M., Fuselier, S. A., et al. 2015, ApJS, 220, 22
McComas, D. J., Zirnstein, E. J., Bzowski, M., et al. 2017, ApJS, 229, 41
Min, K., & Liu, K. 2018, ApJ, 852, 39
Mithaiwala, M., Rudakov, L., & Ganguli, G. 2010, PhPl, 17, 042113
Niemeic, J., Florinski, V., Heerikhuisem, J., & Mishikawa, K.-I. 2016, ApJ,
Parker, E. N. 1963, Interplanetary Dynamical Processes (New York: Wiley-
   Interscience)
Pogorelov, N. V., Fichtner, H., Czechowski, A., et al. 2017a, SSRv, 212, 193
Pogorelov, N. V., Heerikhuisen, J., Mitchell, J. J., Cairns, I. H., & Zank, G. P.
   2009, ApJL, 695, L31
Pogorelov, N. V., Heerikhuisen, J., Roytershteyn, V., et al. 2017b, ApJ, 845, 9
Pogorelov, N. V., Heerikhuisen, J., Zank, G. P., et al. 2011, ApJ, 742, 104
Pogorelov, N. V., Stone, E. C., Florinski, V., & Zank, G. P. 2007, ApJ,
Schwadron, N. A., Bzowski, M., Crew, G. B., et al. 2009, Sci, 326, 966
Schwadron, N. A., & McComas, D. J. 2013, ApJ, 764, 92
Summerlin, E. J., Viñas, A. F., Moore, T. E., Christian, E. R., & Cooper, J. F.
  2014, ApJ, 793, 93
Vasyliunas, V. M., & Siscoe, G. L. 1976, JGR, 81, 1247
Williams, L. L., & Zank, G. P. 1994, JGR, 99, 19229
Witte, M. 2004, A&A, 426, 835
Zirnstein, E. J., Heerikhuisen, J., Funsten, H. O., et al. 2016, ApJL, 818, L18
```